Supplemental Information for: All-optical linear polarization engineering in single and coupled exciton-polariton condensates

I. Gnusov,[1,*] H. Sigurdsson,[2,3,†] J. D. Töpfer,[1] S. Baryshev,[1] S. Alyatkin,[1] and P. G. Lagoudakis[1,3]

[1] *Skolkovo Institute of Science and Technology, Moscow, Territory of innovation center "Skolkovo", Bolshoy Boulevard 30, bld. 1, 121205, Russia.*
[2] *Science Institute, University of Iceland, Dunhagi 3, IS-107, Reykjavik, Iceland*
[3] *School of Physics and Astronomy, University of Southampton, Southampton, SO17 1BJ, UK.*

S1. CONDENSATE POLARIZATION DEPENDENCE ON THE LINEAR POLARIZATION AND ELLIPTICAL OF THE EXCITATION LASER

The experimental data presented in the main manuscript are acquired using a horizontally polarized pump laser which excites the optically trapped polariton condensate. In this supplemental section, we evidence that the linear polarization direction of the pump laser does not affect our presented results. In Fig. S1 we show the measured condensate photoluminescence (PL) Stokes components $S_{1,2,3}$ for varying power and linear polarization direction of the pump laser, the latter being controlled by a half-waveplate (HWP) in the excitation path. The four columns in Fig. S1 correspond to different spatial orientations of the elliptically shaped pump profile (i.e., the optical trap). Figures. S1(a-c) are taken for 0°, (d-f) −45°, (g-i) 90°, and (j-l) 45° degrees of the trap ellipse major axis rotated counterclockwise from the horizontal direction (as defined in the main manuscript). We observe that the condensate polarization always dominantly follows the minor axis of the trap ellipse [see Fig. S1(a),(e),(g), and (k)].

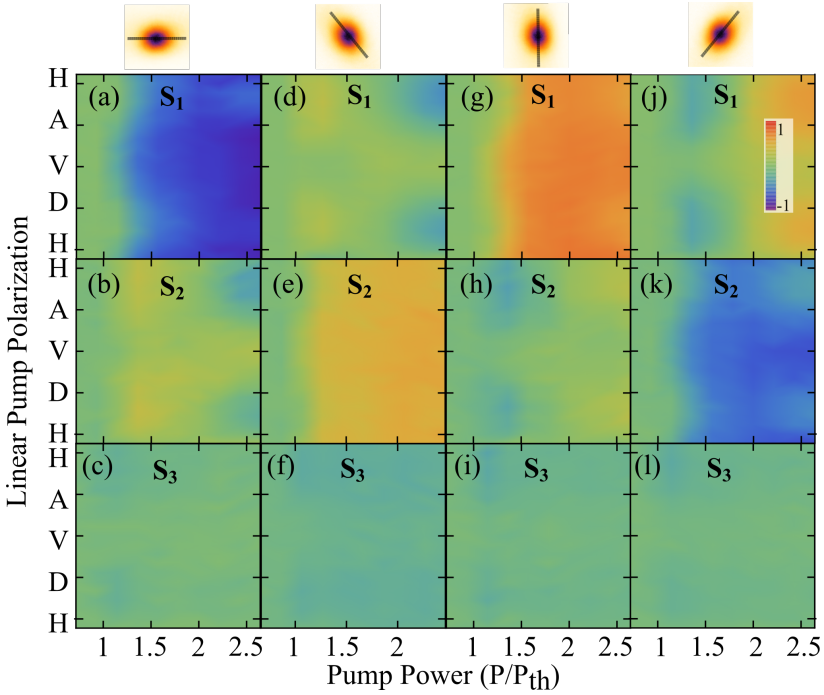

Figure S1. Condensate Stokes components for different pump powers and directions of linear polarization of the excitation laser. The labels H,A,V,D on the vertical axis denote horizontal, antidiagonal, vertical, and diagonal polarization respectively. The condensate PL is depicted on the top row with the black line denoting the trap major axis oriented at (a-c) 0, (d-f) -45, (g-i) 90, and (j-l) 45 degrees with respect to the cavity plane x-axis (horizontal direction).

* I. GnusovIvan.Gnusov@skoltech.ru
† H. Sigurdsson h.sigurdsson@soton.ac.uk

Then we quantitatively investigate the dependence of the condensate polarization on the pump laser ellipticity. We install a quarter waveplate (QWP) in the excitation path so that by rotating the QWP, we can control the ellipticity and handedness of the excitation polarization. In Fig. S2 we show the measured condensate PL Stokes components $S_{1,2,3}$ depending on the pump polarization ellipticity and power. Overall, we obtain a similar behavior of the condensate polarization that was reported for annular optical traps [1].

As expected, circular polarization transfers to the condensate from our nonresonant excitation through the optical orientation of the background excitons feeding the condensate. It can also be seen that the linear polarization of the condensate is sensitive to the pump polarization ellipticity. This is effect is theoretically modeled and discussed further in Sec. S10. In agreement with the findings presented in the main manuscript, when the pump is almost purely linearly polarized (QWP ≈ 0) we observe that the condensate aligns along the short axis of the optical trap [see e.g. blue coloured region in Fig. S2(a)]. Our additional measurements in this supplemental section underline the richness of polarization regimes accessible in polariton condensates where, in this study, we have focused on anisotropic trapping conditions around QWP ≈ 0.

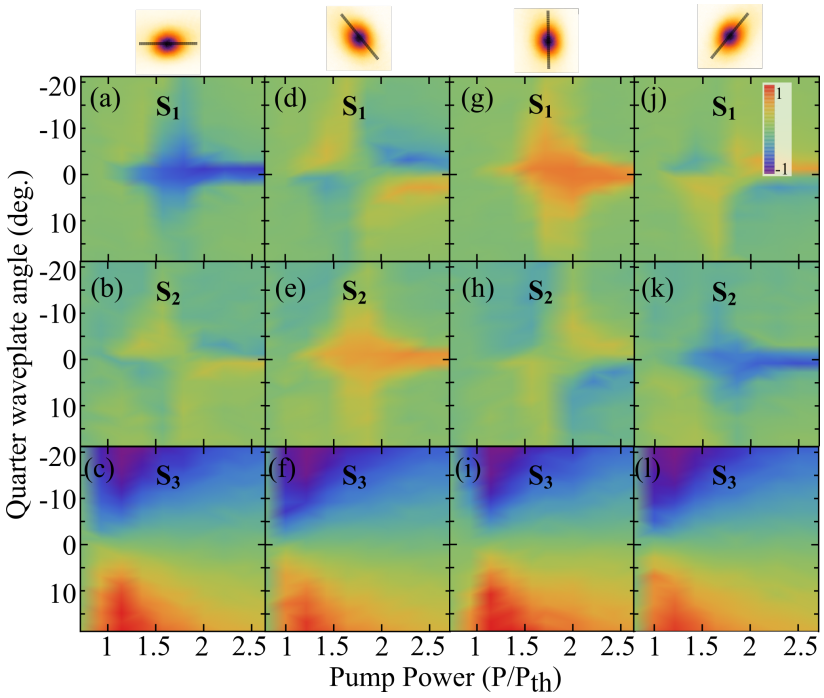

Figure S2. Condensate Stokes components for different pump powers and angles of the QWP (pump polarization ellipticity). The ellipticty of the pump can be written in normalized form as $S_3^{\text{pump}} = \sin(2 \cdot \text{QWP})$. The negative and positive values of the QWP angle correspond to left and right handedness of the circular polarization. The condensate PL is depicted on the top row with the black line denoting the trap major axis oriented at (a-c) 0, (d-f) -45, (g-i) 90, and (j-l) 45 degrees with respect to the cavity plane x-axis (horizontal direction).

S2. COMPENSATION FOR EXPERIMENTAL SETUP OPTICAL RETARDANCE

The birefringence of the optical elements in the detection path of our optical setup gives a rise to circular S_3 polarization component in measured Stokes vector. To illustrate how this detrimental retardance affects our results we show in Fig. S3(a-d) the raw (uncompensated) experimental data for Fig. 3 in the main manuscript.

In the main text we correct for this detrimental polarization ellipticity by applying a Mueller transformation corresponding to the optical elements in the detection path [see Eq. (S1)]. Applying this transformation with appropriately estimated parameters such that the rogue S_3 component in our measurements is minimized [see Fig. S3(d) and S3(e)].

To estimate the the effective retardance axis angle θ of the setup we use the same approach described in [1], giving us $\theta = \pi/2$. We estimate the retardance as $\delta = 0.155\pi$, which considers both the birefringence of the optical elements and the phase shift induced by the mirrors in the detection path. This gives us the following Mueller matrix,

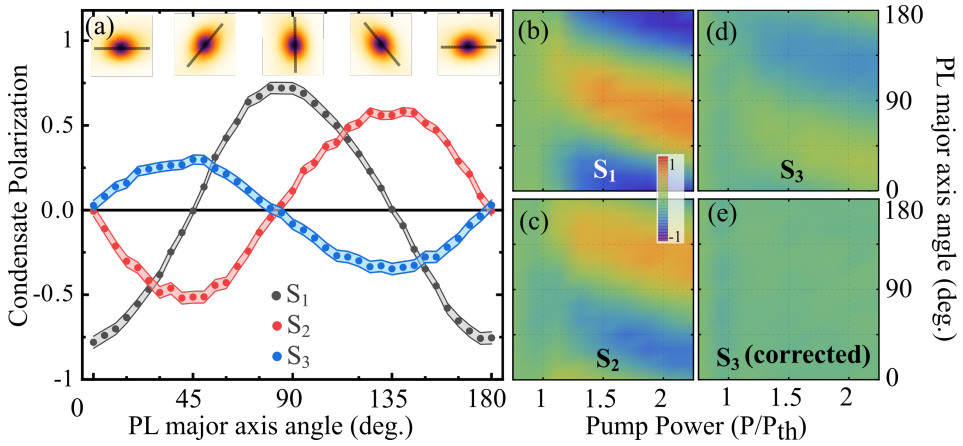

Figure S3. (a)-(d) Raw experimental data without Mueller matrix correction corresponding to the Figure 3 in the main text. (a) Condensate Stokes parameters for different orientations of the condensate major axis in real space (insets) at $P = 1.94P_{th}$. Black lines depict the major axis of the trap. Colored regions show error of the measurement. (b) S_1 , (c) S_2 and (d) S_3 for varying pump powers and major axis orientation. (e) S_3 polarization component of the condensate emission versus trap orientation and pump power corresponding to S_1 and S_2 presented in the main text in Figs. 3(b) and 3(c).

$$\begin{bmatrix} 1 & 0 & 0 & 0 \\ 0 & \cos^2(2\theta) + \sin^2(2\theta)\cos(\delta) & \cos(2\theta)\sin(2\theta)(1-\cos(\delta)) & \sin(2\theta)\sin(\delta) \\ 0 & \cos(2\theta)\sin(2\theta)(1-\cos(\delta)) & \cos^2(2\theta)\cos(\delta) + \sin^2(2\theta) & -\cos 2\theta \sin(\delta) \\ 0 & -\sin(2\theta)\sin(\delta) & \cos(2\theta)\sin(\delta) & \cos(\delta) \end{bmatrix} = \begin{bmatrix} 1 & 0 & 0 & 0 \\ 0 & 1 & 0 & 0 \\ 0 & 0 & 0.8838 & 0.4679 \\ 0 & 0 & -0.4679 & 0.8838 \end{bmatrix} \tag{S1}$$

We finally note that the Mueller transformation does not affect the degree of the polarization (DOP) of the characterized light.

S3. 8-POINT EXCITATION

In this supplemental section, we demonstrate the precise shape of our optical excitation beam is not important as long as it introduces different confinement strengths in the two orthogonal spatial directions. Here, we shape the overall laser profile using 8 Gaussians distributed in the form of an ellipse [see Fig. S4(b)] leading to the formation of an elliptical condensate [see Fig. S4(c)]. In agreement with the results presented in the main text, such an excitation profile also favors the formation of a condensate with linear polarization aligned along the ellipse minor axis. By rotating the excitation profile in the cavity plane Fig. S4(a), we observe the same rotation of the linear polarization of the condensate as in the main text. The deviations from the sinusoidal fits in Fig. S4(a) occur due to a some differences in power and shape of the individual Gaussian spots.

S4. TE-TM SPLITTING

We experimentally measure the TE-TM splitting of the sample by polarization resolving the lower polariton branch in the linear regime (i.e., below condensation threshold) along the k_y momentum axis. We observe that vertically polarized polaritons possess higher energy than horizontally polarized polaritons [see Fig. S5(a)]. The energy difference between these branches gives the TE-TM splitting which follows the expected parabolic trajectory [see Fig. S5(b)].

S5. THE SINGLE-PARTICLE POLARITON HAMILTONIAN

In the non-interacting (linear) regime the polaritons obey the following Hamiltonian (same as Eq. (2) in the main text),

$$\hat{H} = \frac{\hbar^2 k^2}{2m} - \boldsymbol{\sigma} \cdot \boldsymbol{\Omega} + V(\mathbf{r}) - \frac{i\hbar\Gamma}{2}, \tag{S2}$$

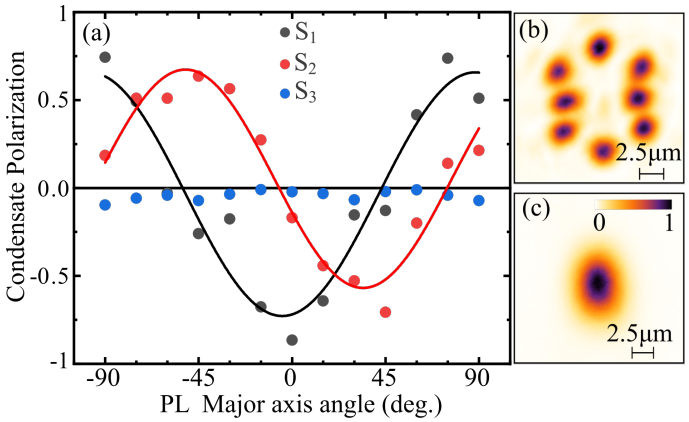

Figure S4. (a) Condensate polarization for different spatial orientations of the 8-Gaussian excitation profile at $P = 2P_{th}$. Red and black curves are the sine fit for the experimental data. (b) Excitation laser intensity profile. (c) Condensate PL.

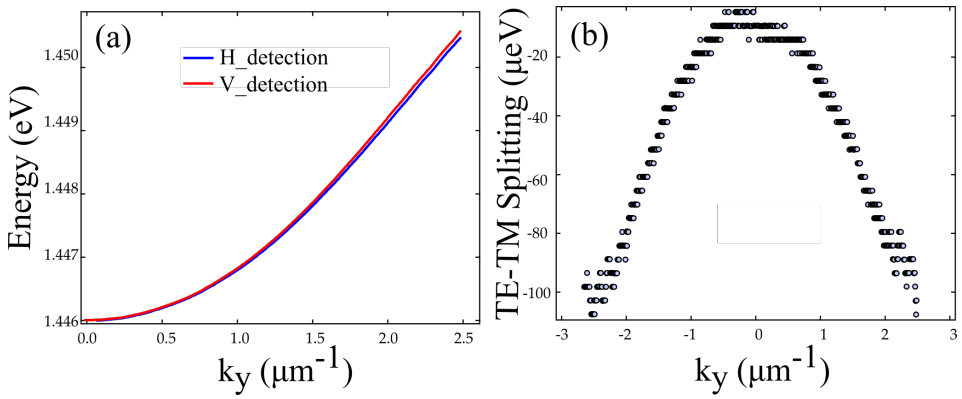

Figure S5. (a) Fitted lower polariton branch in horizontal (blue) and vertical (red) linear polarization detection. (b) Experimentally obtained TE-TM splitting for different wavevectors.

where m is the polariton mass, $\mathbf{k} = (k_x, k_y)$ is the in-plane cavity momentum, Γ^{-1} is the polariton lifetime, $\boldsymbol{\sigma}$ is the Pauli matrix vector, and

$$\boldsymbol{\Omega} = \hbar^2\Delta(k_x^2 - k_y^2,\ 2k_xk_y,\ 0)^T, \tag{S3}$$

is the effective magnetic field [see Fig. S6(e)] coming from the TE-TM splitting of strength Δ. We will consider that our laser generated potential in experiment can be approximated by an elliptically shaped harmonic oscillator (HO),

$$V(\mathbf{r}) = \frac{1}{2}m\omega_x^2x^2 + \frac{1}{2}m\omega_y^2y^2. \tag{S4}$$

Using the shorter momentum operator expression $p_{x(y)} = -i\hbar\partial_{x(y)} = \hbar k_{x(y)}$ for brevity, our Hamiltonian becomes:

$$\hat{H} = \begin{pmatrix} \frac{p_x^2}{2m} + \frac{p_y^2}{2m} + V(\mathbf{r}) - \frac{i\hbar\Gamma}{2} & -\Delta(p_x - ip_y)^2 \\ -\Delta(p_x - ip_y)^{2\dagger} & \frac{p_x^2}{2m} + \frac{p_y^2}{2m} + V(\mathbf{r}) - \frac{i\hbar\Gamma}{2} \end{pmatrix}. \tag{S5}$$

We will diagonalize this problem in the basis of the harmonic oscillator modes written for spin-up and spin-down particles as,

$$|\psi_+\rangle = \sum_{n_x,n_y} c^{(+)}_{n_x,n_y}|n_x, n_y\rangle \tag{S6}$$

$$|\psi_-\rangle = \sum_{n_x,n_y} c^{(-)}_{n_x,n_y}|n_x, n_y\rangle, \tag{S7}$$

where $|n_x, n_y\rangle = |n_x\rangle \otimes |n_y\rangle$ are the harmonic oscillator eigenmodes in the ladder operator $\hat{a}_{x(y)}$ formalism. These are defined in the standard way through the position and momentum operators,

$$x = \sqrt{\frac{\hbar}{2m\omega_x}}(\hat{a}_x^\dagger + \hat{a}_x), \qquad y = \sqrt{\frac{\hbar}{2m\omega_y}}(\hat{a}_y^\dagger + \hat{a}_y), \tag{S8}$$

$$p_x = i\sqrt{\frac{m\hbar\omega_x}{2}}(\hat{a}_x^\dagger - \hat{a}_x), \qquad p_y = i\sqrt{\frac{m\hbar\omega_y}{2}}(\hat{a}_y^\dagger - \hat{a}_y). \tag{S9}$$

Our Hamiltonian can then be expressed,

$$\hat{H} = \begin{pmatrix} \hbar\omega_x\left(\hat{a}_x^\dagger\hat{a}_x + \frac{1}{2}\right) + \hbar\omega_y\left(\hat{a}_y^\dagger\hat{a}_y + \frac{1}{2}\right) - \frac{i\hbar\Gamma}{2} & -\Delta(p_x - ip_y)^2 \\ -\Delta(p_x - ip_y)^{2\dagger} & \hbar\omega_x\left(\hat{a}_x^\dagger\hat{a}_x + \frac{1}{2}\right) + \hbar\omega_y\left(\hat{a}_y^\dagger\hat{a}_y + \frac{1}{2}\right) - \frac{i\hbar\Gamma}{2} \end{pmatrix}, \tag{S10}$$

where the following holds,

$$p_{x(y)}^2 = (p_{x(y)}^2)^\dagger = -\frac{m\hbar\omega_{x(y)}}{2}(\hat{a}_{x(y)}^\dagger\hat{a}_{x(y)}^\dagger - \hat{a}_{x(y)}^\dagger\hat{a}_{x(y)} - \hat{a}_{x(y)}\hat{a}_{x(y)}^\dagger + \hat{a}_{x(y)}\hat{a}_{x(y)}), \tag{S11}$$

$$p_x p_y = (p_x p_y)^\dagger = -\frac{m\hbar\sqrt{\omega_x\omega_y}}{2}(\hat{a}_x^\dagger\hat{a}_y^\dagger - \hat{a}_x^\dagger\hat{a}_y - \hat{a}_x\hat{a}_y^\dagger + \hat{a}_x\hat{a}_y). \tag{S12}$$

The diagonal harmonic oscillator terms can be written more neatly as,

$$E_{n_x,n_y}^{(0)} = \hbar\omega_x\left(n_x + \frac{1}{2}\right) + \hbar\omega_y\left(n_y + \frac{1}{2}\right). \tag{S13}$$

The TE-TM terms will operate on our states as follows,

$$\begin{aligned} p_x^2|n_x, n_y\rangle =& -\frac{m\hbar\omega_x}{2}(\hat{a}_x^\dagger\hat{a}_x^\dagger - \hat{a}_x^\dagger\hat{a}_x - \hat{a}_x\hat{a}_x^\dagger + \hat{a}_x\hat{a}_x)|n_x, n_y\rangle \\ =& -\frac{m\hbar\omega_x}{2}(\sqrt{n_x+1}\sqrt{n_x+2}|n_x+2, n_y\rangle - n_x|n_x, n_y\rangle - (n_x+1)|n_x, n_y\rangle + \sqrt{n_x}\sqrt{n_x-1}|n_x-2, n_y\rangle), \end{aligned} \tag{S14}$$

$$\begin{aligned} p_x p_y|n_x, n_y\rangle =& -\frac{m\hbar\sqrt{\omega_x\omega_y}}{2}(\hat{a}_x^\dagger\hat{a}_y^\dagger - \hat{a}_x^\dagger\hat{a}_y - \hat{a}_x\hat{a}_y^\dagger + \hat{a}_x\hat{a}_y)|n_x, n_y\rangle \\ =& -\frac{m\hbar\sqrt{\omega_x\omega_y}}{2}\Big(\sqrt{(n_x+1)(n_y+1)}|n_x+1, n_y+1\rangle - \sqrt{n_x+1}\sqrt{n_y}|n_x+1, n_y-1\rangle \\ & - \sqrt{n_x}\sqrt{n_y+1}|n_x-1, n_y+1\rangle + \sqrt{n_x n_y}|n_x-1, n_y-1\rangle\Big). \end{aligned} \tag{S15}$$

We will give a special notation to TE-TM terms which do not mix levels,

$$\epsilon_{n_x,n_y} = -\frac{m\hbar\Delta}{2}[\omega_x(2n_x+1) - \omega_y(2n_y+1)]. \tag{S16}$$

We can write a truncated version of our Hamiltonian for just the spins in the trap ground state $|0,0\rangle$ which reads (i.e., coupling to other HO levels is neglected),

$$\hat{H} \approx \begin{pmatrix} E_{0,0}^{(0)} - \frac{i\hbar\Gamma}{2} & \epsilon_{0,0} \\ \epsilon_{0,0} & E_{0,0}^{(0)} - \frac{i\hbar\Gamma}{2} \end{pmatrix}. \tag{S17}$$

The eigenvectors are the horizontally (H) and vertically (V) polarized states of light with eigenvalues,

$$E_{0,0}^{(H,V)} = \frac{\hbar}{2}[\omega_x + \omega_y \mp m\Delta(\omega_x - \omega_y)] - \frac{i\hbar\Gamma}{2}. \tag{S18}$$

We remind that $\Delta < 0$ in our cavity sample [2] (see Fig. S5). This expression confirms experimental observations of the cavity energy resolved emission in Fig. 4(b) in the main text. When the laser induced trap has a major axis along

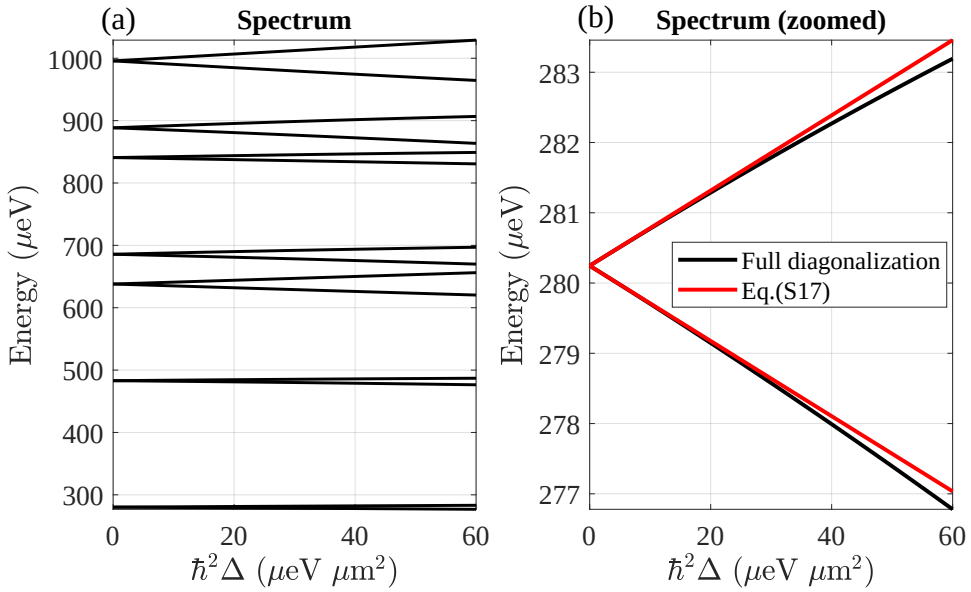

Figure S6. Spectrum of the harmonic oscillator with TE-TM splitting and $\Gamma = 0$ for simplicity. Black lines correspond to diagonalization of Eq. (S10) for $\max(n_{x(y)}) = 15$ and $\omega_x = 1.75\omega_y = 0.55$ ps^{-1} which were estimated from the full-width-half-maximum of the trapped condensate, and for a typical polariton mass of $m = 0.3$ meV ps^2 μm^{-2}. The red lines are outcome of Eq. (S18).

the vertical direction (i.e., $\omega_x > \omega_y$) then we observe higher frequency in the horizontally emitted light as opposed to the vertical light, in agreement with $E^{(H)}_{0,0} > E^{(V)}_{0,0}$. When $\omega_x < \omega_y$ the vice versa appears. In Fig. S6 we put $\Gamma = 0$ for simplicity and compare the calculated spectrum obtained from diagonalizing Eq. (S10) (black lines) for $\max(n_{x(y)}) = 15$ modes against our truncated lowest HO level Hamiltonian Eq. (S18). The generalization of Eq. (S17) to arbitrary angles of the potential orientation in the x-y plane is straightforward and presented in Eq. (4) in the main text.

S6. GENERALIZED GROSS-PITAEVSKII SIMULATIONS

We will now model the dynamics of the polariton condensate spinor $\Psi = (\psi_+, \psi_-)^T$ using the generalized (driven-dissipative) Gross-Pitaevskii equation, coupled to a semiclassical rate equation describing a reservoir of low-momentum excitons $\mathbf{X} = (X_+, X_-)^T$ which scatter into the condensate [3]:

$$\begin{aligned} i\hbar\frac{\partial\psi_\pm}{\partial t} &= \left[-\frac{\hbar^2\nabla^2}{2m} - \Delta(p_x \mp ip_y)^2 + g\left(X_\pm + \frac{P}{W}\right) + \alpha|\psi_\pm|^2 + i\hbar\frac{RX_\pm - \Gamma}{2}\right]\psi_\pm, \\ \frac{\partial X_\pm}{\partial t} &= P - (R|\psi_\pm|^2 + \Gamma_R)X_\pm + \Gamma_s(X_\mp - X_\pm). \end{aligned} \tag{S19}$$

Here, ∇^2 denotes the two-dimensional Laplacian operator, Δ the TE-TM splitting, m is the polariton effective mass, g and α are the repulsive (defocusing) interaction constants describing the polariton-reservoir and polariton-polariton blueshift, R governs the stimulated scattering from the reservoir into the condensate, Γ and Γ_R are the polariton and active exciton decay rates, and Γ_s is the rate of spin relaxation. As we are working in continuous wave regime, and the pump is linearly polarized at all times, we do not need to take into account the polarization- and time-dependence of a high-momentum (inactive) reservoir describing excitons that are too energetic to scatter into the condensate [4]. Instead, the contribution of photoexcited high-momentum excitons to the condensate appears through the blueshift term P/W where W describes the conversion rate of high-momentum excitons into low-momentum excitons $X_\pm$ that sustain the condensate.

We will use the pseudospin formalism (analogous to the Stokes parameters describing the cavity photons) to describe

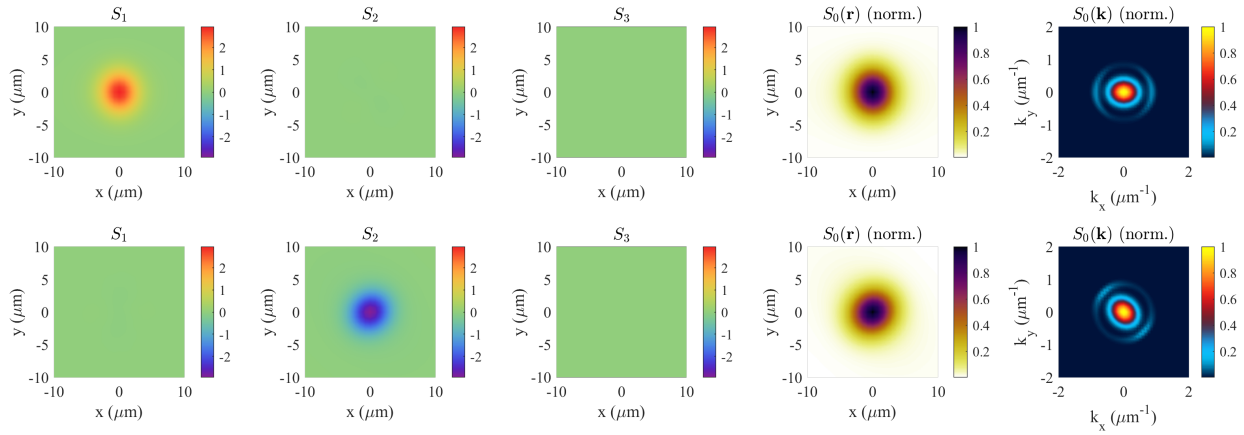

Figure S7. (Top row) Steady state solution from simulation of Eq. (S19). Here we used the $P_I(\mathbf{r})$ pump profile with a major axis along the vertical direction, $b/a = 1.3$. The results show a condensate forming with horizontal polarization implying occupation of the excited trap spin state. (Bottom row) Same simulations but now the pump major axis is orientated $\pi/4$ from the horizontal resulting in antidiagonally polarized condensate which again corresponds to the excited spin state of the trap.

the polarization of the condensate (note that in Eq. (1) in the main manuscript we have used the normalized definition),

$$\mathbf{S} = \begin{pmatrix} S_1 \\ S_2 \\ S_3 \end{pmatrix} = \Psi^\dagger \boldsymbol{\sigma} \Psi. \tag{S20}$$

Here, $\boldsymbol{\sigma}$ is the Pauli matrix vector and the total density of the condensate is expressed as $S_0 = |\psi_+|^2 + |\psi_-|^2$.

We will study the dynamics of Eq. (S19) for three different excitation profiles shown in Figs. S8(a,d,f). The profiles shown in Fig. S8(d) and S8(f) represent the experimental configurations shown in Fig. 1(a,b) in the main manuscript and in Fig. S4(b). We also introduce, for completeness, a third type of an elliptical excitation profile in the numerical analysis shown in Fig. S8(a). The three excitation profiles can be written as follows,

$$P_I(\mathbf{r}) = P_0 \frac{L_I^4}{\left(\frac{x^2}{a^2} + \frac{y^2}{b^2} - r_0^2\right)^2 + L_I^4}, \tag{S21}$$

$$P_{II}(\mathbf{r}) = P_0 \frac{L_{II}^4}{\left(x^2 + y^2 - r_0^2\right)^2 + L_{II}^4} [1 - \eta \cos\left(2\varphi + \phi_{\text{maj}}\right) \sin^2\left(\pi r / 2 r_0\right)], \tag{S22}$$

$$P_{III}(\mathbf{r}) = P_0 \sum_{n=1}^{8} \frac{L_{III}^2}{(x - x_n)^2 + (y - y_n)^2 + L_{III}^2}. \tag{S23}$$

Here, $L_{I,II,III}$ denote the spread (thickness) of the potentials. For pumps (S21) and (S22) the common radius r_0 defines the length of the ellipse minor and major axis. Specifically, the minor and major axis are given by the parameters $0 < a, b < 1$ for (S21) and η, ϕ_{maj} for (S22). For the third pump profile (S23) we use coordinates x_n, y_n of the eight tightly focused pump spots corresponding to the experiment. The laser power density is given by P_0.

In Fig. S7 we show the obtained steady state wavefunction Ψ obtained from random initial conditions while driving the system above the pump threshold $P_0 > P_{\text{th}}$ using the first pump profile $P_I(\mathbf{r})$. The threshold P_{th} is defined as the transition point where the normal state $|\Psi| = 0$ becomes unstable and instead a condensate forms $|\Psi| > 0$. Indeed, choosing parameters corresponding to the experiment we obtain complete match between experimental observations and simulations. Testing 100 different random initial conditions we find that the simulated condensate always converges to a steady state corresponding to the excited spin state of the trap. The parameters of the simulation are: $m = 0.3$ meV ps^2 μm^{-2}; $\Gamma = \frac{1}{5.5}$ ps^{-1}; $\hbar\alpha = 3$ μeV μm^2, $g = \alpha$; $\Gamma_R = \Gamma/4$; $R = 0.67\alpha$; $W = 0.05$ ps^{-1}; $\Gamma_s = \Gamma_R/2$; $\hbar^2\Delta = -0.03$ meV μm^2; $L_I = 5$ μm; $L_{II} = 6$ μm; $L_{III} = 2$ μm; $r_0 = 5$ μm; $\eta = 0.2$; and $P_0 = 4.625$ μm^{-2} ps^{-1} which is around $\approx 20\%$ above threshold for each configuration.

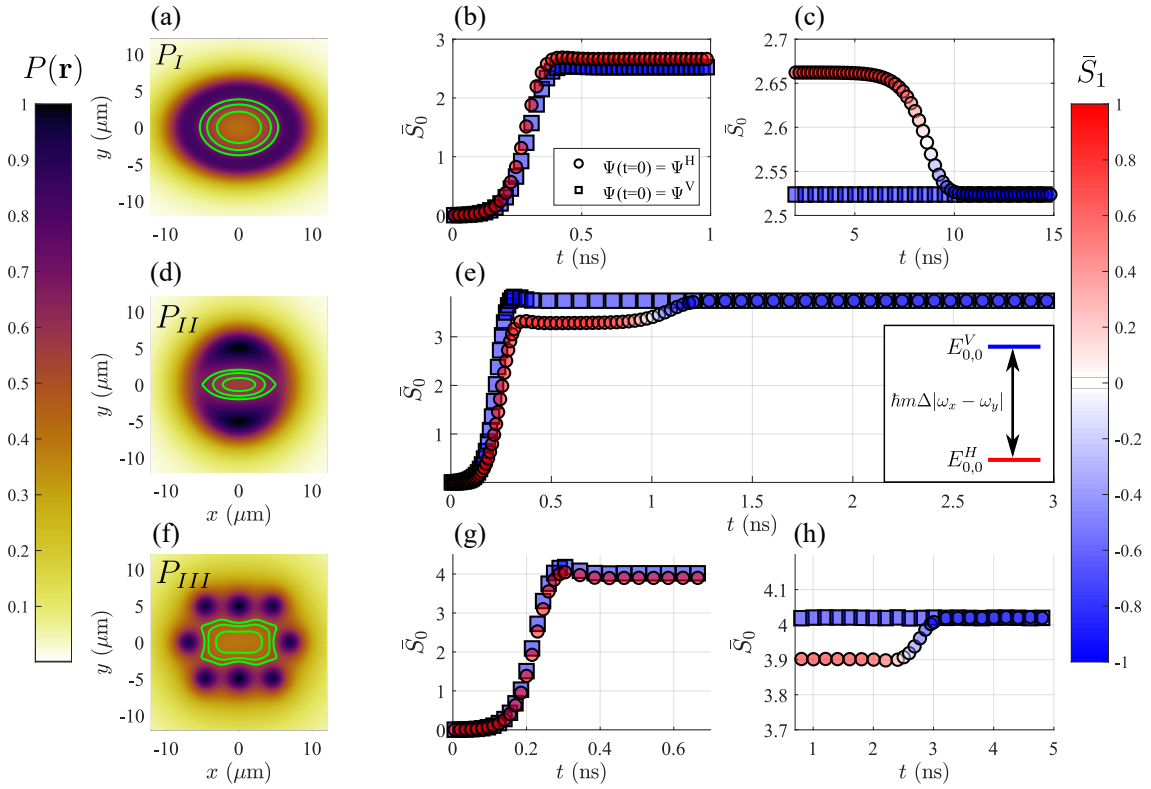

Figure S8. (a,d,f) Pump profiles (normalized) corresponding to Eqs. (S21)-(S23). In (a) we have set $a/b = 1.4$ and in (d) $\phi_{\text{maj}} = 0$ and $\eta = 0.2$. The green lines are contours which represent the isoenergy lines of the optical trap. The inset in (e) shows schematically the energy structure of the linearly polarized modes in the trap s-orbital. In the panels on the right we show the corresponding condensate $\bar{S}_0$ dynamics for the two ansatz $\Psi^{H,V}$ in Eq. (S24) separately (circles and squares respectively) for fixed pumping value P_0 above threshold. The red-blue color denotes the area-integrated linear polarization $\bar{S}_1$. In panels (b,c) and (g,h) we split the time axis to better show the early and late dynamics. In panel (b) the early dynamics show that the Ψ^H ansatz rises faster and the condensate saturates into a horizontally polarized state (red circles) with higher particle number as compared to the vertically polarized state (blue squares), implying it has larger gain. At later times shown in panel (c), the horizontal polarized solution always collapses into the vertically polarized solution, indicating that it is only metastable and that a vertically polarized condensate survives at long times. In panels (e) and (g) we observe a qualitatively different early dynamics where now the horizontally polarized condensate rises slower. Eventually, as we see in (e) and (h), the horizontally polarized solution destabilizes and converges into a vertically polarized condensate.

A. Condensate metastability

We will here scrutinize the early and late condensate dynamics using two simple initial conditions (ansatz). We will use a trap with a horizontal major axis (i.e., $\omega_x < \omega_y$) since all other major axis orientations are completely generalizable. The two initial conditions for Eq. (S19) are written,

$$\Psi(t=0) = \Psi^{H,V} = Ae^{-c(x^2+y^2)} \begin{pmatrix} 1 \\ \pm 1 \end{pmatrix}. \tag{S24}$$

The parameter c is chosen to have $\Psi^{H,V}$ localized dominantly within the trap and $A \ll 1$ is a small number to minimize nonlinear effects in the initial dynamics. We then solve Eq. (S19) for each initial condition and plot the spatially integrated particle number S_0 and S_1 (normalized) Stokes parameter as a function of time,

$$\bar{S}_0(t) = \frac{1}{\mathcal{A}} \int_{\mathcal{A}} S_0(\mathbf{r},t) d\mathbf{r} \qquad \bar{S}_1(t) = \frac{\int_{\mathcal{A}} S_1(\mathbf{r},t) d\mathbf{r}}{\int_{\mathcal{A}} S_0(\mathbf{r},t) d\mathbf{r}}, \tag{S25}$$

where $\mathcal{A}$ is the area enclosed by the pump profile ridge (i.e., $\max P(\mathbf{r})$).

Simulations using the generalised Gross-Pitaevskii equation (S19) for fixed power P_0 (above threshold) and the three pump profiles $P_{I,II,III}$ are shown in Figs. S8(b,c), and S8(e), and S8(g,h), respectively. We plot the area-integrated particle number $\bar{S}_0$ for the two different initial conditions $\Psi^{H,V}$ (circles and squares, respectively). The color of the markers indicates the area-integrated linear polarization $\bar{S}_1$ of the condensate. In Figs. S8(b,c) and S8(g,h) we split the time axis to show better the early and late dynamics. The inset in Fig. S8(e) shows schematically the energy splitting between the polarizations. For pump profiles P_{II} and P_{III} we see that in the early dynamics a vertically polarized condensate (blue squares) rises faster and saturates at a higher particle number than a horizontally polarized condensate (red circles). This can be understood from the fact that the vertical and horizontal polarized modes of the condensate have different effective masses and, thus, have different penetration depths into the gain region of the pump. In particular, pumps P_{II} and P_{III} lead to an excess density of reservoir excitons about the short axis of the ellipse. Since the penetration depth of the confined mode in the potential well is larger in the direction of the linear polarization axis, this would increase the overlap of the mode co-polarized with the short-axis of the potential well with the gain region, i.e. the 'excited state' in the fine structure. In the late dynamics [Fig. S8(e) and S8(h)] the horizontal solution destabilizes and converges into the vertically polarized solution. This is in agreement with our experimental observations showing robust condensation into the excited spin state of the optical traps.

Interestingly, for pump P_I the early dynamics [Fig. S8(b)] are reversed with respect to $P_{II,III}$. Now the horizontally polarized condensate rises faster and saturates at a higher particle number. This pump profile does not generate a strong excess of excitons about the ellipse short axis and, as a consequence, the higher energy polaritons, co-polarized with the short axis, escape (leak) faster from the trap. Nevertheless, in the late dynamics [Fig. S8(c)] the horizontally polarized solution destabilizes and collapses into the vertically polarized solution. This observation underlines that the stable solution of the condensate does not necessarily correspond to the one with maximum particle number $\bar{S}_0$. In the next section we address the different parameters of our model that determine the stability of the excited state and the ground state.

S7. STABILITY ANALYSIS ON A TWO MODE PROBLEM

Here, we will analyse the stability properties of the condensate by projecting our order parameter on only the lowest trap state $|0,0\rangle$. Let us here denote $\psi_\pm(\mathbf{r},t) \to \psi_\pm(t)$ as the condensate order parameter describing polaritons only in the HO ground state and neglect contribution from higher HO modes,

$$\begin{aligned} i\frac{d\psi_\pm}{dt} &= \left[\alpha|\psi_\pm|^2 + gX_\pm + i\frac{RX_\pm - \Gamma}{2}\right]\psi_\pm + (\epsilon + i\gamma)\psi_\mp, \\ \frac{dX_\pm}{dt} &= P - \left(\Gamma_R + R|\psi_\pm|^2\right)X_\pm + \Gamma_s(X_\mp - X_\pm). \end{aligned} \tag{S26}$$

The parameters here have the same meaning as their counterparts in Eq. (S19), but we stress that we have absorbed $\hbar$ into their definition for brevity and some will obtain modified values after integrating out the spatial degrees of freedom depending on the precise shape of the condensate and reservoir. We have removed the P/W term as it only induces an overall blueshift to both spins which does not affect the stability properties of the system. The spin-coupling parameter ϵ corresponds to $\epsilon_{0,0}$ from Eq. (S16). We additionally include an imaginary coupling parameter γ which physically represents different linewidths of the horizontal and vertical polarized modes (i.e., different decay rates).

The two steady state solutions of interest correspond to spin-balanced reservoirs $X_+ = X_-$ supporting either purely horizontally or vertically polarized condensate written,

$$\Psi_{\rm st}^{H,V} = \sqrt{\frac{S_0^{H,V}}{2}}\begin{pmatrix}1\\ \pm 1\end{pmatrix}e^{-i\omega^{H,V}t} \tag{S27}$$

where,

$$\omega^{H,V} = \frac{\alpha}{2}S_0^{H,V} + gX^{H,V} \pm \epsilon_{0,0}, \qquad S_0^{H,V} = \frac{P}{\Gamma \mp 2\gamma} - \frac{\Gamma_R}{R}, \qquad X^{H,V} = \frac{\Gamma \mp 2\gamma}{R}. \tag{S28}$$

The power to reach the lower threshold solution is $P_{\rm th} = \Gamma_R(\Gamma - 2|\gamma|)/R$. The stability analysis of the $\Psi_{\rm st}^{H,V}$ solutions is exactly the same as in Ref. [5] where a 5×5 Jacobian matrix $\mathbf{J}$ corresponding to linearisation of Eq. (S26) around its steady state solutions was derived. This allows determining the stability of the solutions in terms of their Jacobian eigenvalues λ_n (also known as *Lyapunov exponents* in nonlinear dynamics or *Bogoliubov elementary excitations* in the context of Bose-Einstein condensates). If a single eigenvalue of $\mathbf{J}$ has a positive real part then the solution is said to

be *asymptotically unstable*. It was found in Ref. [5] that the relative strength between the mean field energy coming from the condensates $\alpha|\psi_\pm|^2$ and the reservoir blueshift $gX_\pm$ played a big role in whether the excited state or the ground state was stable.

To understand this better, we will first consider the stability of the two solutions $\Psi_{\rm st}^{H,V}$ using a more general coupled Gross-Pitaevskii equations (similar to coupled amplitude oscillators),

$$i\frac{d\psi_\pm}{dt} = \alpha|\psi_\pm|^2\psi_\pm + \epsilon\psi_\mp, \qquad \epsilon > 0. \tag{S29}$$

Clearly, $\Psi_{\rm st}^{H,V}$ is a solution of the above equation for any particle number $S_0 = S_0^H = S_0^V$ with frequency $\omega^{H,V} = \alpha S_0/2 \pm \epsilon$. The Lyapunov exponents of these solutions are written:

$$\begin{aligned}
\lambda_1^{H,V} &= 0, \\
\lambda_2^{H,V} &= \sqrt{2\epsilon(-2\epsilon \pm \alpha S_0)}, \\
\lambda_3^{H,V} &= -\sqrt{2\epsilon(-2\epsilon \pm \alpha S_0)}.
\end{aligned} \tag{S30}$$

We only have three eigenvalues because our two level system (S29) can be described with the three-dimensional pseudospin state vector [see Eq. (S20)], analogous to the Stokes vector of light. It is clear that only $\lambda_2^{H,V}$ can have real values greater than zero (the signature of instability) and there are only two cases when this happens:

1. If $\alpha > 0$ (repulsive particle interactions) then $\mathrm{Re}(\lambda_2^H) > 0$ when $\alpha S_0 > 2\epsilon$.
2. If $\alpha < 0$ (attractive particle interactions) then $\mathrm{Re}(\lambda_2^V) > 0$ when $|\alpha S_0| > 2\epsilon$.

This simple result shows that the stability of the excited state and the ground state changes when the mean field energy αS_0 exceeds the fine structure splitting 2ϵ. In our case, polariton interactions are repulsive $\alpha > 0$ and the condensate should always form in the ground state when $S_0 > 2\epsilon/\alpha$ [6]. Note that $2\hbar\epsilon \approx 20$ μeV in our experiment which is small compared to the typical polariton mean field energies αS_0. It therefore appears puzzling that we observe stable excited state condensation when the above simple consideration dictates that only the ground state should be stable.

In the following, we will address two different mechanisms that fight against ground state condensation. **First,** if the ground state is lossier than the excited state (i.e., $\gamma/\epsilon < 0$) then polaritons will preferentially condense into the excited state until S_0 exceeds a critical value [5]. However, as we can see from Fig. S8(b,c), even if the excited state is lossier than the ground state the condensate can still preferentially populate and stabilize in the excited state. **Second,** a stable excited spin state condensation can appear due to an effective attractive nonlinearity coming from the reservoir [i.e., the term $gX_\pm$ in Eq. (S26)]. Indeed, it is well established that the presence of the condensate "eats away" the reservoir density analogous to the hole burning effect in lasers [7]. In the adiabatic regime where the reservoir is assumed to adjust to the condensate density dynamics very fast it can be approximated as follows,

$$X_\pm = \frac{P}{\Gamma_R}\left[1 - \frac{R|\psi_\pm|^2}{\Gamma_R} + \mathcal{O}(|\psi_\pm|^4)\right]. \tag{S31}$$

The nonlinearity of the condensate can therefore described by an effective interaction parameter,

$$\alpha_{\rm eff} = \alpha - \frac{gPR}{\Gamma_R^2}. \tag{S32}$$

To test our hypothesis, we numerically solve the eigenvalues of the Jacobian for Eq. (S26) and plot their maximum real part for the $\Psi_{\rm st}^{H,V}$ solutions in Fig. S9 (red and blue curves, respectively) as a function of varying α and several values of Γ_R [Fig. S9(a)] and γ [Fig. S9(b)]. Indeed, we see that there exist three distinct regimes which we schematically illustrate with the blue-white-red color gradient:

i. Ground state unstable and excited state stable.

ii. Both states stable.

iii. Ground state stable and excited state unstable.

As expected from Eq. (S32), the stability range of the excited state increases as Γ_R decreases [see Fig. S9(a)] due to the nonlinearity $\alpha_{\rm eff}$ becoming more negative. Moreover, the stability range of the excited state also increases when γ/ϵ becomes more negative corresponding to the ground state becoming lossy [see Fig. S9(b)]. We point out

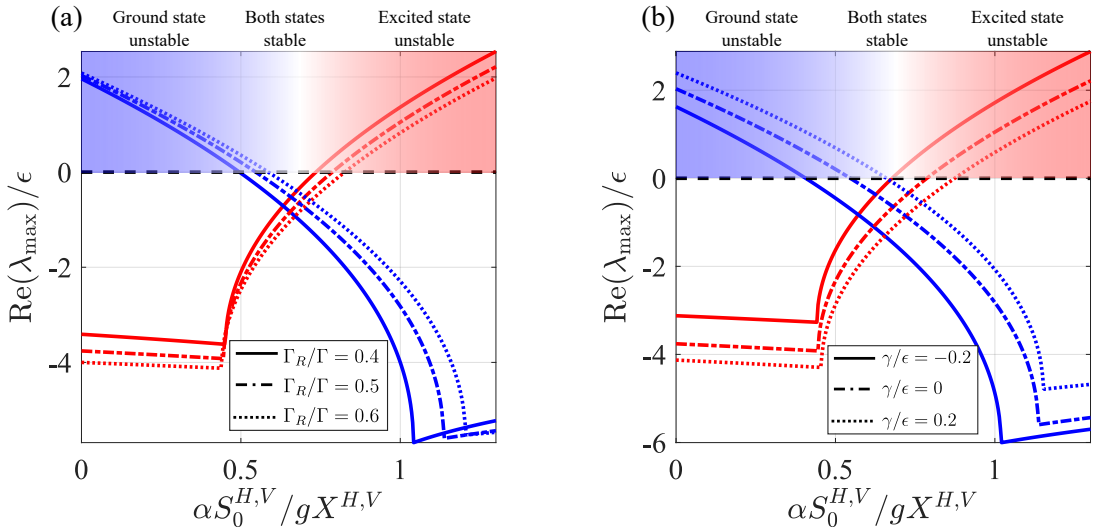

Figure S9. Maximum real eigenvalues (Lyapunov exponents) from the Jacobian of Eq. (S26) around the two steady state solution $\Psi_{\mathrm{st}}^{H,V}$ (red and blue curves, respectively) for $\epsilon = 1/20$. Regimes where $\mathrm{Re}(\lambda_{\mathrm{max}}) > 0$ imply instability of the solution. The color gradient at the top is added for illustration purposes. Parameters in units of Γ: $\Gamma_s = 1/4$, $\epsilon = 1/20$, $R = 0.015$, $g = 5R/6$, and $P = 2P_{\mathrm{th}}$. In (a) we fix $\gamma = 0$ and in (b) we fix $\Gamma_R = 0.5$.

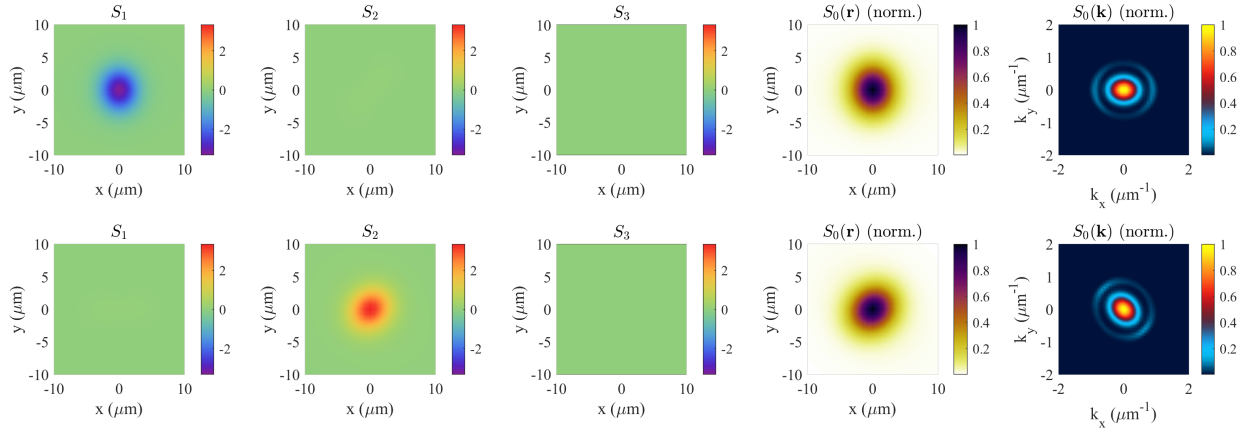

Figure S10. Same simulations as in Fig. S7 but with doubled interactions strength $\alpha \to 2\alpha$ (keeping all other parameters unchanged) such that the excited spin state now becomes unstable and only the ground state becomes populated.

that it is not possible to determine separately the contribution of $\alpha S_0^{H,V}$ and $gX^{H,V}$ in experiment since we can only measure the net blueshift in condensate energy. Nevertheless, our experimental results indicate that the current pump configuration favours the far-left regime in Fig. S9 where the ground state is unstable. Recently, we reported results corresponding to the far-right regime where robust ground state condensation was instead observed [1] using the same cavity sample but somewhat different experimental configuration. How exactly one can tune from one regime to the other is difficult to tell, but the clearest path would either involve changing the detuning between the photon and exciton mode. This is possible because $\alpha \propto |\chi|^4$ and $g \propto |\chi|^2$ where $|\chi|^2$ is the exciton Hopfield fraction of the polariton quasiparticle. Another method would be to design an excitation profile $P(\mathbf{r})$ which changes the mean field rate R of particles scattering into the condensate.

Finally, to see if our hypothesis agrees with the full spatial calculations of Eq. (S19) we repeat the simulation from Fig. S7 in a new Fig. S10 with the strength of polariton-polariton interactions doubled, i.e. $\alpha \to 2\alpha$ while keeping all other parameters unchanged. We now find, in agreement with our predictions, that the steady state solution (tested over 100 random initial conditions) converges to the spin ground state instead of the excited state. This can be evidenced from the opposite polarization appearing in the Stokes components in Fig. S10 as compared to Fig. S7.

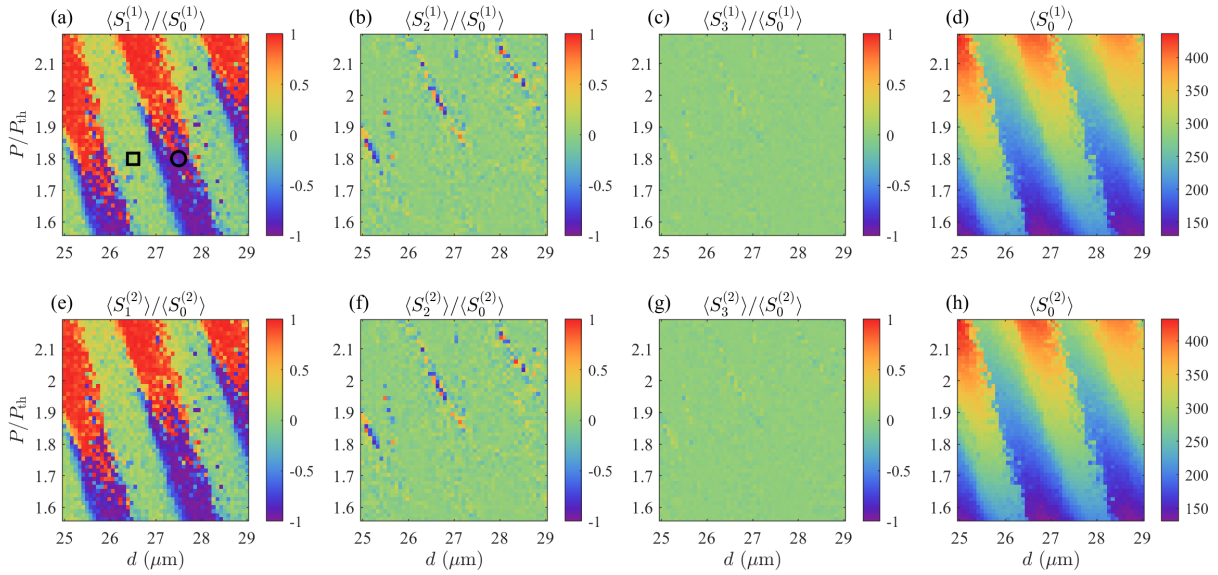

Figure S11. (a-d) Time averaged Stokes parameters of $\psi_{\pm}^{(1)}$ and (e-h) $\psi_{\pm}^{(2)}$ from random initial conditions and varying pump power P and distance d. We normalise the pump power in units of the threshold power for a single condensate $P_{\rm th} = (\Gamma - 2|\gamma|)\Gamma_R/R$. The parameters of the simulation are: $\epsilon = -0.01$ ps^{-1}; $\gamma = \epsilon/2$; $\Gamma_R = \Gamma/4$; $\Gamma_s = \Gamma_R/2$; $\alpha = 0.15\epsilon$; $R = 0.05\epsilon$; $\omega_0 = 5.5\Gamma$; $g = \alpha$; $m = 0.3$ meV ps^2 μm^{-2}; $J_0 = 0.67e^{1.8i}$ ps^{-1}; and $\mathcal{J} = 0.2J$

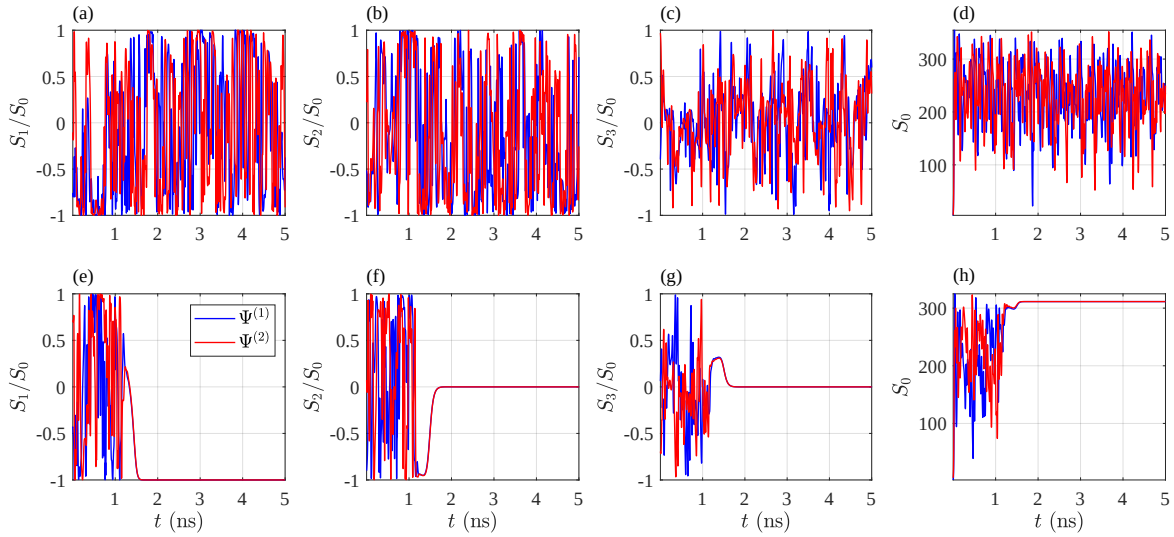

Figure S12. Evolution of the Stokes parameters for a single realization of the coupled condensates at the (a-d) the black square and (e-h) the black circle in Fig. S11, corresponding to the unstable and stable regimes, respectively.

S8. SUPPLEMENTAL NUMERICAL DATA FOR COUPLED SPINOR CONDENSATES

In this section we provide additional numerical data to Fig. 6 [given in Figs. S11 and S12] in the main manuscript for completeness and some additional details on the numerical method. The angled brackets of the Stokes parameters $\langle S_n^{(1,2)}\rangle$ represent time-average. We applied a constant step size Bogacki-Shampine algorithm [8] (a 3rd order Runge-Kutta). The timestep was chosen $\Delta t = 0.05$ ps and the integration was over $T = 5000$ ps for each condensate realization.

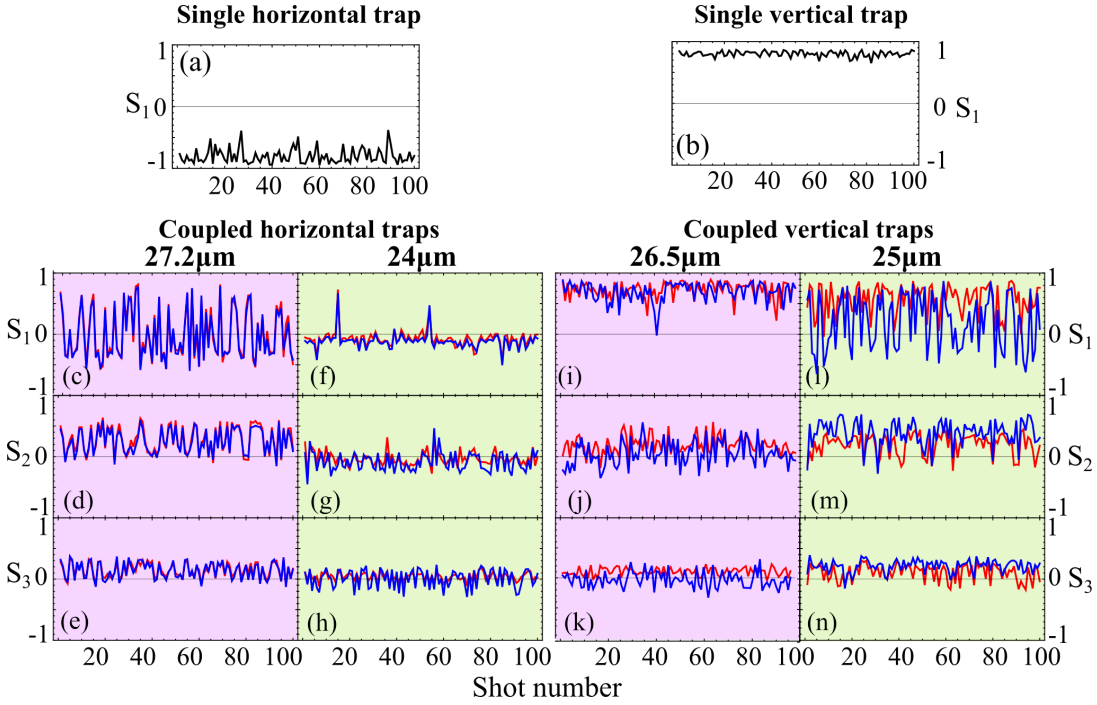

Figure S13. 100 realizations (shots) of the condensates Stokes components time-integrated in each 50 μs excitation shot. (a) and (b) shows S_1 of single horizontally and vertically elongated condensate (trap) respectively. S_1, S_2, and S_3 for two coupled condensates with their trap's major axes orientated longitudinally to the coupling direction and separated by 27.2 μm (c)-(e) and 24 μm (f)-(h), respectively. S_1, S_2, and S_3 for two coupled condensates with their trap's major axes orientated perpendicularly to the coupling direction, separated by 26.5 μm (i)-(k) and 25 μm (l)-(n), respectively. Blue and red colors correspond to right and left condensate respectively. Background green and purple colors depict different coupling regimes.

S9. ADDITIONAL EXPERIMENTAL DATA FOR COUPLED CONDENSATES

Here we present additional experimental data on the coupled elliptical condensates. In this experiment, we measure the Stokes components for 100 quasi-CW 50 μs shots. Each experimental point in Fig. S13 represents the polarization component averaged within one excitation shot. We note that the S_1, S_2 and S_3 in Figs. S13(c)-(n) are not measured simultaneously but consequently under the same pumping conditions and at the same position on the sample.

As expected, when isolated, the individual condensates stay dominantly polarized linearly parallel to the minor axis of the pump trap, as we describe in the main text [see Figs. S13(a) and S13(b) for a horizontal trap and vertical trap, respectively]. However, some fluctuations can be sometimes observed, for example, in the horizontally elongated trap in Fig. S13(a). This happens due to some noise in our system as well due to mode competition. It is worth noting that such fluctuations decrease the values of the Stokes components presented in Figs. 2-4 in the main text since there we integrate/average over hundreds of shots.

In Figs. S13(c)-(h) we present the Stokes components for coupled horizontally elongated ellipses separated by 27.2 μm in Figs. S13(c)-(e) and 24 μm in Figs. S13(f)-(h). Blue and red colors correspond to the "right" and "left" condensate, respectively. For 27.2 μm, the condensate flips randomly from horizontal to vertical polarization from shot-to-shot, whereas the S_2 has smaller values (less than 0.5) but also flips from shot to shot. Overall the S_3 component stays close to zero. For a different separation distance 24 μm shown in Figs. S13(f)-(h) we observe that all Stokes components are close to zero in each shot. This means that the condensate pseudospin fluctuates rapidly in time within one excitation pulse with a zero mean polarization just like in simulation in Figs. S12(a)-(d). Notice that the Stokes components still remain correlated indicating the condensate are coupled together.

We also plot all polarization components for two coupled vertically elongated condensates [Figs. S13(i)-(n)]. The weaker coupling of such mutual trap configuration is evidenced through less correlations between the left and right condensates (i.e., the red and blue curves fluctuate more independently). For a distance of 26.5μm both condensates have strong horizontal polarization — i.e. big S_1 component and small S_2 and S_3 components. This corresponds to Figs. S12(e)-(h) in simulations. At a distance of 25 μm the condensates are in a semi-depolarized regime with oscillating S_1 and S_2 from shot to shot, and small S_3.

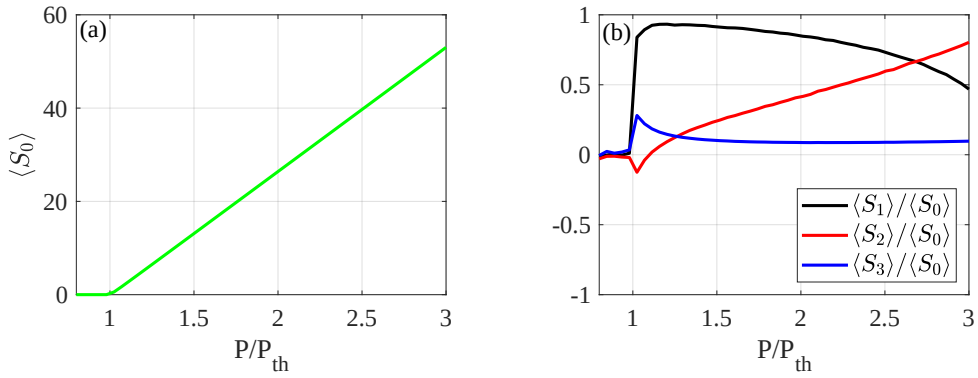

Figure S14. Time-integrated Stokes (pseudospin) components of the simulated condensate under spin-imbalanced pumping. Each datapoint is averaged over 1000 random initial conditions. Parameters in units of Γ are given: $P_+/P_- = 1.0355$, $P = (P_+ + P_-)/2$, $P_{\rm th} = (\Gamma - 2|\gamma|)\Gamma_R/R$, $\Gamma_R = 1/5$, $\Gamma_s = \Gamma_R/4$, $\epsilon = 1/40$, $\gamma = 0$, $R = 0.015$, $W = 2\Gamma_R$, and $g = R/2$.

S10. POWER DEPENDENT PSEUDOSPIN ROTATION

In this section we explain the results of Fig. 3(b) and 3(c) in the main manuscript where we can observe noticeable change in the linear polarization of the condensate as we increase the power. It manifests as counterclockwise rotation of the pseudospin in the equatorial plane of the Poincaré sphere.

The explanation for the power dependent pseudospin rotation is due to slight polarization ellipticity in the excitation laser. This creates an imbalance between the spin-up and spin-down exciton populations in the system and a consequent out-of-plane effective magnetic field $\Omega_\perp < 0$ which results in additional torque on the pseudospin $\dot{\mathbf{S}} = \mathbf{S} \times \mathbf{\Omega}$. We note however that instead of persistent pseudospin precession around the magnetic field $\mathbf{\Omega}$ (as one would expect in the linear regime) the pseudospin is stationary in Gross-Pitaevskii simulations. This means that the small amount of torque coming from the ellipticity in the excitation beam is gradually rotating the pseudospin fixed point on the Poincaré sphere. A more detailed analysis on this power dependent rotation of the fixed points will be pursued elsewhere.

This is confirmed through Gross-Pitaevskii simulations using Eq. (S26) where we introduce a slight pumping imbalance by redefining a spin-dependent pumping rate $P \to P_\pm$ where $P_+ \neq P_-$. We present our simulation in Fig. S14 where we show the time-integrated Stokes (pseudospin) components of the condensate at increasing mean pump power $[P = (P_+ + P_-)/2]$ where each datapoint is averaged over 1000 random initial conditions. We have set $P_+/P_- = 1.0355$ and other parameters of the model (specified in the caption) are taken similar to the ones used in Fig. S9 and S11. We point out that Eq. (S26) must now include the additional pump induced blueshift $gP_\pm/W$ like in Eq. (S19) since it contributes to $\mathbf{\Omega}_\perp$. The results show precisely the counterclockwise rotation of the pseudospin in the (S_1, S_2) plane like in Fig. 3(b) and 3(c) in the main manuscript. We have also confirmed that if $P_+ < P_-$ then the pseudospin rotates clockwise in the (S_1, S_2) plane.

Moreover, this change in the S_1 and S_2 can also be evidenced from the experimental data presented in Fig. S2. There, a small change in the polarization ellipticity of our excitation beam dramatically affects the S_1 and S_2 distributions.

[1] I. Gnusov, H. Sigurdsson, S. Baryshev, T. Ermatov, A. Askitopoulos, and P. G. Lagoudakis, Optical orientation, polarization pinning, and depolarization dynamics in optically confined polariton condensates, Phys. Rev. B **102**, 125419 (2020).

[2] M. Maragkou, C. E. Richards, T. Ostatnický, A. J. D. Grundy, J. Zajac, M. Hugues, W. Langbein, and P. G. Lagoudakis, Optical analogue of the spin hall effect in a photonic cavity, Opt. Lett. **36**, 1095 (2011).

[3] M. Wouters and I. Carusotto, Excitations in a nonequilibrium Bose-Einstein condensate of exciton polaritons, Phys. Rev. Lett. **99**, 140402 (2007).

[4] C. Antón, T. C. H. Liew, G. Tosi, M. D. Martín, T. Gao, Z. Hatzopoulos, P. S. Eldridge, P. G. Savvidis, and L. Viña, Energy relaxation of exciton-polariton condensates in quasi-one-dimensional microcavities, Phys. Rev. B **88**, 035313 (2013).

[5] H. Sigurdsson, Hysteresis in linearly polarized nonresonantly driven exciton-polariton condensates, Phys. Rev. Research **2**, 023323 (2020).

[6] I. A. Shelykh, Y. G. Rubo, G. Malpuech, D. D. Solnyshkov, and A. Kavokin, Polarization and propagation of polariton condensates, Physical Review Letters **97**, 066402 (2006).

[7] E. Estrecho, T. Gao, N. Bobrovska, M. D. Fraser, M. Steger, L. Pfeiffer, K. West, T. C. H. Liew, M. Matuszewski, D. W. Snoke, A. G. Truscott, and E. A. Ostrovskaya, Single-shot condensation of exciton polaritons and the hole burning effect, Nature Communications **9**, 2944 (2018).

[8] V. Flunkert, Delay differential equations, in *Delay-Coupled Complex Systems: and Applications to Lasers* (Springer Berlin Heidelberg, Berlin, Heidelberg, 2011) pp. 153–163.